(Received 13 November 2025, Accepted 13 January 2026, Scheduled 30 January 2026)

Compact Dual-Polarized Endfire Dielectric Resonator Antenna for 5G Millimeter-Wave Terminal Application

Xiao-Mei Ni[1] and Xin-Hao Ding[2,*]

[1] School of Aeronautic Engineering, Nanjing University of Industry Technology, Nanjing 210023, China
[2] School of Information Science and Technology, Nantong University, Nantong 226019, China

ABSTRACT: This work presents a miniaturized dual-polarized endfire dielectric resonator antenna (DRA) array tailored for millimeter-wave (mmWave) 5G terminal systems. The proposed antenna element integrates a dielectric resonator with a cavity structure, both realized using standard printed circuit board (PCB) fabrication. Two orthogonal resonant modes of the DRA are excited to generate vertical (VP) and horizontal (HP) polarizations. To achieve broadband characteristics, two orthogonal cavity modes are further introduced and coupled with the DRA modes, enabling dual-mode operation. The VP and HP elements utilize an identical physical configuration, ensuring a highly compact architecture. Based on this unit, a four-element array was designed, fabricated, and experimentally verified. Measurements confirm an operational bandwidth of 26.1–29.8 GHz for both polarization states, with peak gains of 10.0 dBi and 10.1 dBi for VP and HP, respectively. Furthermore, both polarizations demonstrate beam-steering capability, indicating that the proposed dual-polarized endfire DRA array is a promising solution for next-generation 5G mmWave terminal applications.

1. INTRODUCTION

With the rapid evolution of the fifth-generation (5G) mobile communication networks, the demand for higher data throughput and ubiquitous connectivity under the Internet of Everything (IoE) paradigm has dramatically increased [1–3]. For compact terminal platforms, the microwave spectrum has become congested and spatially limited. By contrast, millimeter-wave (mmWave) bands offer wide spectral resources and low transmission latency, enabling much higher channel capacities [4, 5]. Consequently, mmWave antenna design has attracted tremendous research interest. To overcome propagation attenuation and realize wide angular coverage, beam-scanning array antennas are indispensable [6]. In addition, dual polarizations are crucial to ensuring link reliability and improving spectral efficiency [7]. Although various dual-polarized endfire antennas have been reported, their applicability to compact mmWave terminals is often limited by large size, high profile, or poor integration. While dielectric resonator antennas (DRAs) offer low loss and flexible modal control, most mmWave DRA-based endfire designs remain single-polarized.

Compared with conventional dual-polarized broadside antennas, dual-polarized endfire configuration is particularly advantageous for mobile terminals, as it minimizes the interference caused by hand effects [8]; therefore, it represents a valuable and meaningful research direction. A variety of dual-polarized endfire arrays supporting beam scanning have been developed using different techniques. For instance, [9] reported an mmWave dual-polarized array combining horizontal (HP) and vertical (VP) dipoles within a single structure. A chain-slot configuration is adopted in [10], where HP and VP were individually excited. However, integrating such feeding structures on a unified substrate remains challenging. In [11], two quasi-Yagi antennas, each with a dedicated port, are compactly integrated to achieve dual polarizations. Several studies [12–15] present dual-polarized endfire phased arrays employing dipole radiators for HP and substrate integrated waveguide (SIW) elements for VP. In [16], a dipole fed by an open-ended SIW provides VP radiation, while a bent strip line coupled slot generates HP radiation. Likewise, [17] uses a combination of an open-ended SIW with two-stage grating strips for VP and V-shaped dipoles fed by a grounded coplanar waveguide for HP. Although these architectures achieve high integration, VP and HP components are still independently designed, and their feeding structures [11–14, 16] or required clearance areas [15, 17] often result in large planar footprints. In [10, 11], magneto-electric (ME) dipole antennas are introduced to reduce the footprint, but their inherent electromagnetic properties lead to relatively high profiles. A compact dual-polarized endfire array is realized in [20] by utilizing a shared open-ended cavity, where VP and HP were generated by the cavity and slot modes, respectively. Nevertheless, the cavity slot caused structural asymmetry, producing a radiation pattern tilt.

For mmWave frequencies, dielectric resonator antennas (DRAs) are particularly appealing due to their compact geometry, low dielectric loss, and flexible modal design [21–23]. In [24], an HP endfire substrate-integrated DRA is developed by employing metallic sidewalls and central air vias to realize dual-beam radiation. A compact VP endfire antenna operating at mmWave bands was reported in [25], where slot and cavity modes are combined with a DRA mode to broaden the bandwidth. A VP substrate-integrated DRA array merging with a microwave antenna was proposed in

* Corresponding author: Xin-Hao Ding (xhding1@hotmail.com).

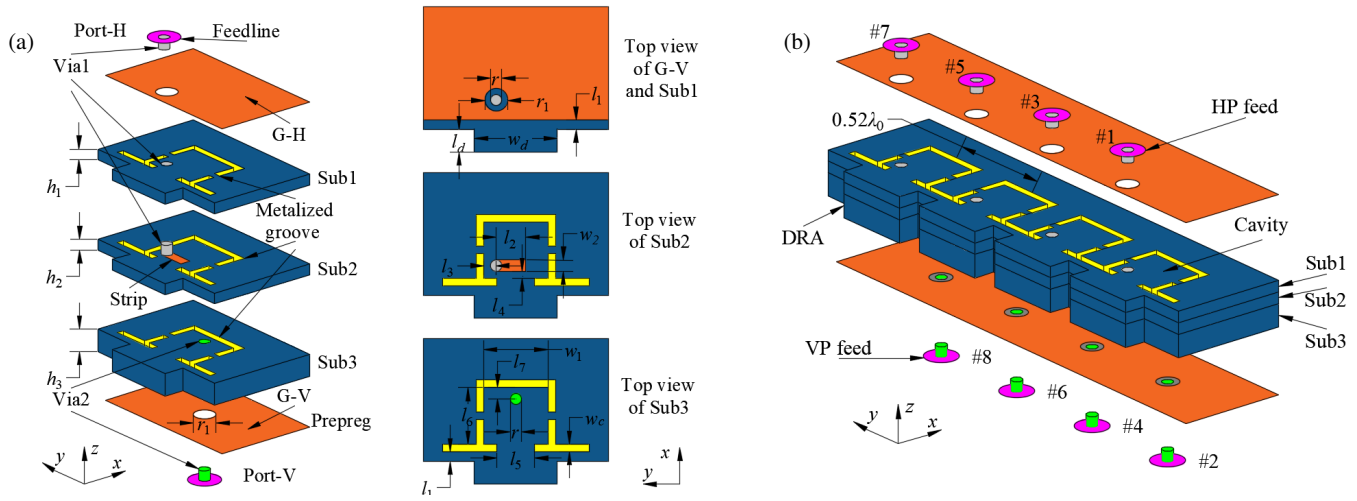

FIGURE 1. Structure of the proposed antenna. (a) Structure of the element, (b) structure of the array. (Design parameters: $l_1 = 0.5$, $l_2 = 1.05$, $l_3 = 0.5$, $l_4 = 0.4$, $l_5 = 2$, $l_6 = 3$, $l_7 = 0.6$, $l_d = 1.2$, $w_1 = 3.4$, $w_2 = 0.4$, $w_d = 4.4$, $r = 0.15$, $r_1 = 1.25$, $h_1 = 0.625$, $h_2 = 0.625$, $h_3 = 1.27$. Units: mm.)

[26]. A dual-polarized, dual-band hybrid DRA is described in [27]; however, its radiation is broadside-oriented. From these studies, it is evident that most mmWave endfire DRAs remain single-polarized [24–26]. Hence, to exploit the full advantages of DRAs and achieve high structural integration, a new design strategy for dual-polarized substrate-integrated endfire DRAs is required.

In this paper, a compact dual-polarized mmWave endfire DRA array based on substrate integration is presented. Two orthogonal DRA modes are independently excited to realize VP and HP polarizations. The VP mode is generated through open-ended cavity coupling, while the HP mode is excited via a metallic strip connected to a probe. To further extend the operational bandwidth and cover relevant commercial frequency ranges, two orthogonal cavity modes are incorporated and merged with their corresponding DRA modes, enabling dual-mode excitation for each polarization. Finally, a four-element array is designed and fabricated, exhibiting beam-scanning behavior in both polarizations. The proposed configuration establishes a practical foundation for future highly integrated dual-polarized endfire DRA designs.

2. ANTENNA STRUCTURE

The structure of the proposed dual-polarized endfire DRA is presented in Fig. 1. The antenna consists of three stacked RF-60TC substrates ($\varepsilon_r = 6.15$, $\tan\delta = 2 \times 10^{-3}$), labeled Sub1, Sub2, and Sub3. Two metallic ground layers, denoted as G-V and G-H, are employed for the horizontal (HP) and vertical (VP) polarizations, respectively. Together with the metallized groove, they create an open-ended metallic cavity. This cavity, coupled with the DRA positioned at its aperture, forms a complete radiating element. Notably, both VP and HP radiations are produced by the same physical configuration. Separate excitation paths are used for the two polarizations. Metallic vias, referred to as Via1 and Via2, link the respective feeding networks. For VP excitation, the signal from Port-V is delivered through Via1 into the cavity, thereby coupling energy to the DRA. In contrast, HP excitation is achieved through Via2, which connects to a metallic stripline that guides energy from Port-H to the DRA. Based on this single element, a dual-polarized four-element array is designed, as shown in Fig. 1(b). Each polarization employs four independently fed ports: the lower set of ports corresponds to VP, while the upper set corresponds to HP.

3. ANTENNA DESIGN

3.1. Antenna Element Design

The design of the antenna element plays a pivotal role in realizing a millimeter-wave dual-polarized endfire array capable of beam steering. The fundamental concept is to exploit two orthogonal resonant modes within the dielectric resonator to generate dual-polarized radiation. To enhance structural compactness and facilitate system-level integration, a substrate featuring a high dielectric constant is selected for the DRA implementation. As illustrated in Fig. 2, the vertical polarization (VP) and horizontal polarization (HP) are independently produced through two distinct feeding configurations, corresponding to Case 1 and Case 2, respectively. Case 3 represents the integrated configuration, formed by the combination of the two preceding cases.

The resonant frequency of the rectangular DRA operating in the TE_{111} mode can be approximately estimated using the dielectric waveguide model. The formula is as follows:

$$f_{\mathrm{TE}_{111}} = \frac{c}{2\sqrt{\varepsilon_r}}\sqrt{\left(\frac{1}{a}\right)^2 + \left(\frac{1}{b}\right)^2 + \left(\frac{1}{h}\right)^2}$$

Here, c represents the speed of light in a vacuum. a, b, and h denote the length, width, and height of the DRA, respectively. $a = l_d$, $b = w_d$, and $h = h_1 + h_2 + h_3$.

3.1.1. VP Design

The vertical polarization (VP) configuration is illustrated in Case 1 in Fig. 2. As depicted, the VP feeding system is composed of two main components: a metallic cavity (formed by metallized grooves together with the upper and lower metal layers) and a feeding probe (Via2). The radio frequency (RF) energy for VP excitation is supplied through Port-V. The signal propagates along Via2, which drives the metallic cavity, and subsequently, the excited cavity electromagnetically couples energy into the adjacent DRA to generate VP radiation.

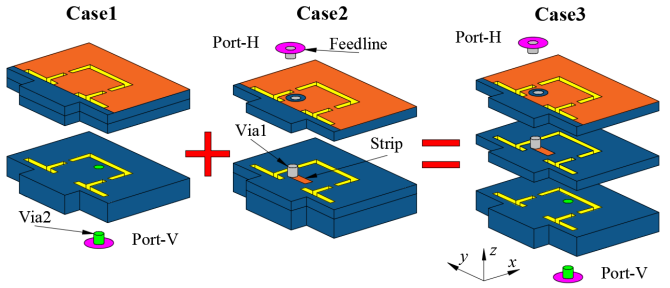

FIGURE 2. Design process of the element.

The operational principle and associated electric field distribution for the VP antenna are shown in Fig. 3(a). The dominant resonant mode inside the DRA is identified as TE^{y}_{111}. To extend the impedance bandwidth, an additional cavity mode, namely TE^{x}_{111}, is introduced to operate jointly with the DRA mode, thereby achieving a dual-mode response. The simulated performance of the VP radiator is presented in Fig. 4(a), demonstrating a -10 dB impedance bandwidth of approximately 13.9% (26.0–29.9 GHz) and a peak gain of 5.5 dBi at 29.3 GHz. The radiation pattern at 28 GHz, as shown in Fig. 4(b), confirms stable directional performance.

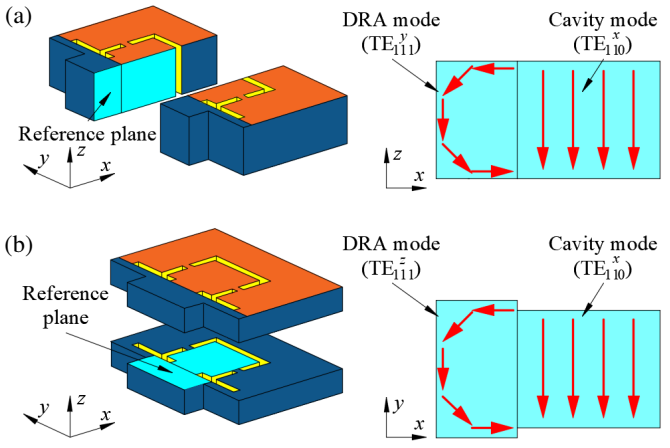

FIGURE 3. E-field distribution in the reference plane. (a) TE^{y}_{111} mode and TE^{x}_{110} mode for VP. (b) TE^{z}_{111} mode and TE^{x}_{110} mode for HP.

To validate the interaction mechanism between the DRA and the cavity, a parametric investigation was carried out. Fig. 6 depicts the variation of $|S_{11}|$ with respect to changes in DRA and cavity dimensions. Adjusting the DRA width (w_1) shifts the first resonant frequency without affecting the second, whereas modifying the cavity length (l_d) alters the second resonant mode while leaving the first unchanged. These results verify

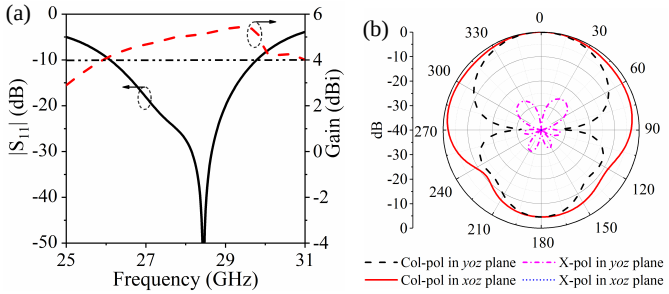

FIGURE 4. Performance of VP element. (a) Simulated $|S_{11}|$ and gain, (b) simulated radiation pattern at 28 GHz.

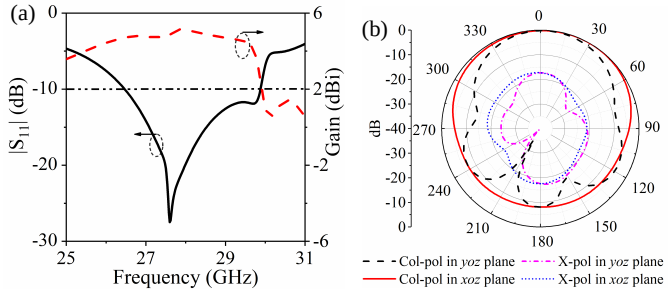

FIGURE 5. Performance of HP element. (a) Simulated $|S_{11}|$ and gain, (b) simulated radiation pattern at 28 GHz.

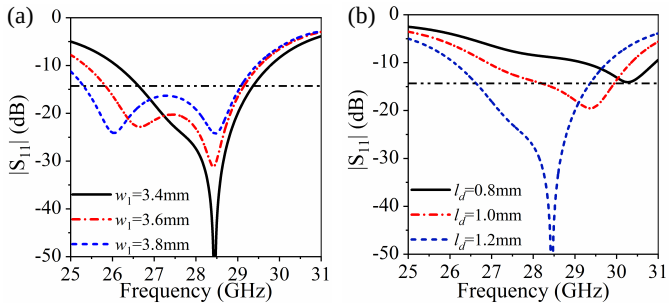

FIGURE 6. Effect of (a) w_1, (b) l_d on $|S_{11}|$ of VP element.

that the first resonance originates from the DRA mode and the second from the cavity mode.

3.1.2. HP Design

The horizontal polarization (HP) configuration is illustrated in Case 2 in Fig. 2. The HP excitation network is composed of three components, namely a metallic via (Via1), a microstrip line, and the feeding strip. Power is delivered from Port-H, transmitted through Via1, and subsequently coupled to the DRA by the attached strip to generate HP radiation.

The operating principle and simulated electric field distribution of the HP antenna are depicted in Fig. 3(b). The dominant resonant mode within the DRA corresponds to the TE^{z}_{111} mode. To achieve a broader impedance bandwidth, an additional cavity mode (TE^{x}_{111}) is incorporated and combined with the DRA mode, leading to dual-mode operation. It should be emphasized that although both VP and HP utilize the TE^{x}_{110} cavity mode designation, their respective electric field orientations differ — aligned along the y-axis for VP and along the z-axis for HP.

The simulated results of the HP element are shown in Fig. 5. As seen in Fig. 5(a), the antenna provides an impedance bandwidth of 12.5% (26.4–29.9 GHz) with a maximum realized gain of 5.2 dBi at 27.8 GHz. The radiation pattern at 28 GHz, presented in Fig. 5(b), confirms desirable endfire radiation performance.

To substantiate the mode analysis, a parametric investigation was carried out, as illustrated in Fig. 7. Changes in the DRA width (w_1) primarily shift the second resonant mode while leaving the first mode nearly unchanged, whereas variations in the cavity length (l_d) predominantly affect the first mode. These results verify that the first resonance originates from the cavity mode, while the second corresponds to the DRA mode.

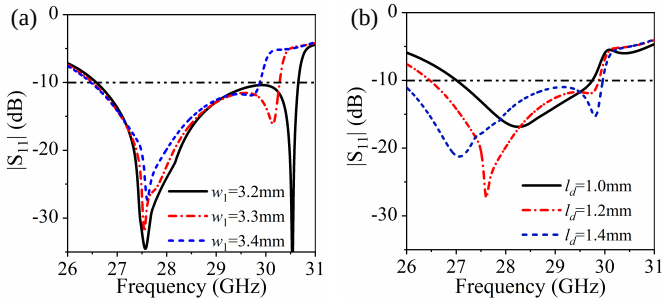

FIGURE 7. Effect of (a) w_1, (b) l_d on $|S_{11}|$ of HP element.

3.1.3. Study on the Interaction between VP and HP

In the configuration depicted as Case 3 in Fig. 2, both the VP and HP feeding networks are integrated within the same structure, necessitating an investigation of their mutual coupling behavior. The simulated characteristics of this combined design are presented in Fig. 8. The two polarizations exhibit an overlapping impedance bandwidth of 12.1% (26.3–29.7 GHz), while maintaining an isolation level exceeding 15 dB between Port-V and Port-H. The influence of cross-feeding is analyzed in Fig. 9. As shown in Fig. 9(a), variations in the parameter l_1 associated with the VP feed have a minimal impact on the HP impedance response, indicating negligible interference from the VP network. Similarly, from Fig. 9(b), adjustments to l_4 in the HP feed do not noticeably affect the VP bandwidth. Consequently, it can be concluded that the two feed structures operate with high electrical independence, and the coupling between VP and HP is effectively suppressed. The use of a single, unified dielectric resonator and cavity structure enables dual

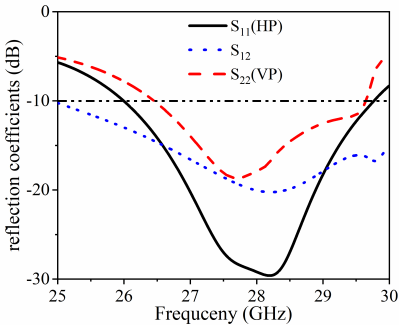

FIGURE 8. Performance of Case 3.

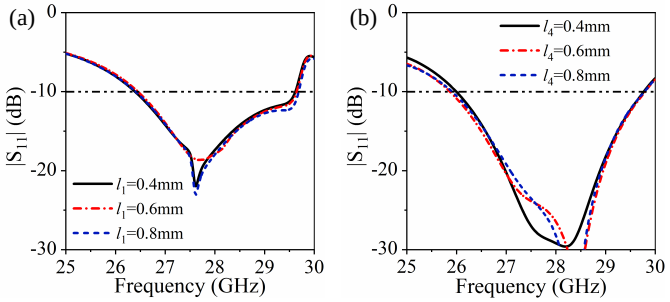

FIGURE 9. Effect of (a) l_1, (b) l_4 on $|S_{11}|$ of Case 3.

polarizations, eliminating the need for separate footprints and inherently improving integration.

It further details how the synergistic coupling between orthogonal DRA modes and cavity modes serves as the fundamental physical mechanism for achieving wideband performance, leveraging the parametric studies (e.g., Figs. 6 and 7) to substantiate this. The comparison with prior art is now more interpretative, explicitly contrasting our co-designed, compact DRA-based approach with designs that use independent radiators, thereby highlighting the superior structural integration and miniaturization achieved in this work.

Dual-mode operation serves as the core mechanism for bandwidth enhancement. For each polarization, the bandwidth is achieved by coupling a fundamental DRA mod with an additional cavity mode (TE_{110}). The parametric studies in Fig. 6 and Fig. 7 are directly referenced to substantiate this, showing that the DRA geometry primarily controls the first resonance while the cavity dimensions tune the second. This synergistic coupling between two orthogonal resonant paths effectively merges two adjacent bands, resulting in a wider impedance bandwidth than that of using a single mode.

3.2. Four-Element Antenna Array

Building upon the previously developed dual-polarized endfire DRA unit, a 1×4 linear array is implemented, as illustrated in Fig. 1(b). The center-to-center distance between adjacent elements is set to $0.52\lambda_0$, where λ_0 denotes the free-space wavelength at 28 GHz. Each antenna element is individually excited through its own feed port, which facilitates beam-steering capability across the array. The simulated inter-port performance, presented in Fig. 10, reveals that all ports maintain mutual isolation levels exceeding 15 dB, confirming excellent decoupling between the array channels.

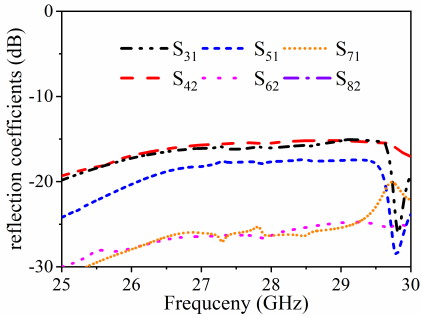

FIGURE 10. Simulated S-parameters of the array.

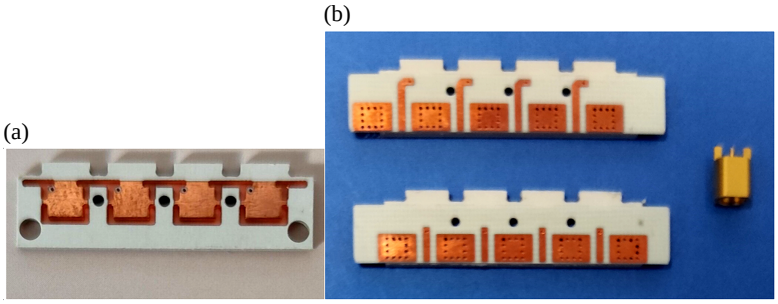

FIGURE 11. Photograph of the antenna prototype. (a) Antenna board. (b) From top to bottom: feeding board for HP and VP, special mm-Wave connector.

4. SIMULATION & MEASURED RESULTS

To validate the proposed design, a prototype of the antenna was fabricated and experimentally characterized. The fabricated model is presented in Fig. 11, demonstrating a highly compact and well-integrated structural configuration. The three substrate layers are aligned using mechanical alignment holes and fixed through standard PCB lamination and bonding processes. The metallized vias and ground planes ensure accurate electrical alignment between layers, while the stacked substrates are mechanically secured during fabrication to maintain structural integrity and alignment accuracy.

4.1. Measured Results of VP

Figure 12(a) shows both measured and simulated reflection coefficients and gains when Port-V is excited. The measured impedance bandwidth of -10 dB is 13.9%, which spans from 25.9 GHz to 29.9 GHz. Meanwhile, the simulated bandwidth is 13.5% (from 26.1 GHz to 29.9 GHz). The slight difference between the measured S_{11} responses of the two ports arises from asymmetric excitation paths, fabrication tolerances, and weak mutual coupling between orthogonal modes. Within the operating bandwidth range, the measured gain varies between 8.8 dBi and 10.0 dBi, which is slightly below the simulated gain ranging from 8.9 dBi to 10.3 dBi. The corresponding radiation performances on both the *xoy*-plane and *xoz*-plane at 28 GHz are depicted in Fig. 13(a). The radiation patterns show a strong agreement between measured and simulated results. On the *xoy*-plane, the two beams' maximum radiation is directed at elevation angles of 0° and 25°, respectively. This indicates that in the case of VP radiation, good beam scanning capability can be achieved.

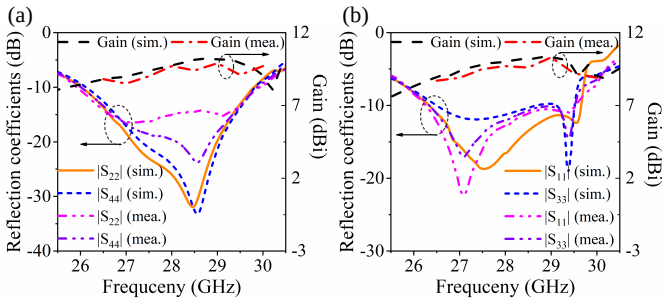

FIGURE 12. Simulated and measured reflection coefficients and gains of the antenna prototype. (a) VP. (b) HP.

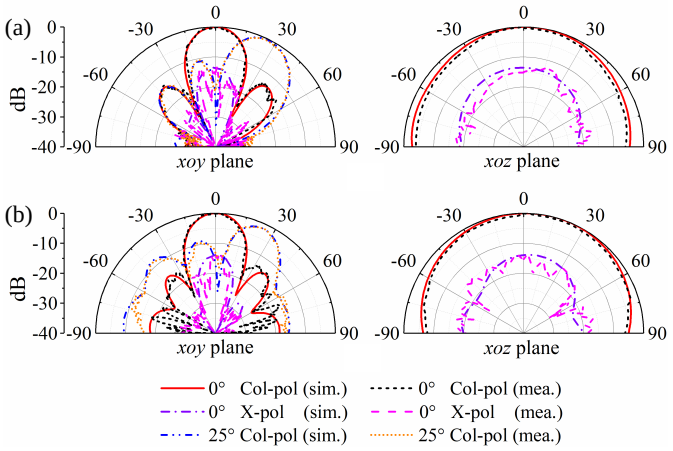

FIGURE 13. Simulated and measured radiation patterns of the DRA array. (a) VP. (b) HP.

4.2. Measured Results of HP

Figure 12(b) shows both measured and simulated reflection coefficients and gains when Port-V is excited. The measured impedance bandwidth of -10 dB is 13.3%, which spans from 26.1 GHz to 29.8 GHz. Meanwhile, the simulated bandwidth is 12.1% (from 26.3 GHz to 29.7 GHz). Within the operating bandwidth range, the measured gain varies between 8.7 dBi and 10.1 dBi, which is slightly below the simulated gain ranging from 9.0 dBi to 10.3 dBi. The corresponding radiation performances on both the *xoy*-plane and *xoz*-plane at 28 GHz are depicted in Fig. 13(b). The radiation patterns show a strong agreement between measured and simulated results. On the *xoy*-plane, the two beams' maximum radiation is directed at elevation angles of 0° and 25°, respectively. This indicates that in the case of VP radiation, the good beam scanning capability can be achieved. The fabrication errors are inherently unavoidable in practice. To mitigate their impact, two measures are adopted. First, high-precision fabrication processes are employed to minimize dimensional inaccuracies. Second, multiple antenna prototypes are fabricated and independently measured, and the consistency among the measured results is used to verify the reliability and correctness of the experimental data.

TABLE 1. Performance comparison with the previous antenna designs.

Ref.	Published Year	f_0 (GHz)	Over lapping BW (%)	Gain (dBi) (VP/HP)	Electrical Dimension (λ_0^3) (Number of elements)	Polarization	Antenna Type (VP/HP)
[15]	2023	27	16.3	10.0/10.3	$0.74 \times 2.7 \times 0.23$ (4)	Dual	SIW/Dipole
[16]	2023	27	14.6	9.3/9.7	$0.81 \times 2.28 \times 0.15$ (4)	Dual	SIW/Slot
[17]	2024	27	24	13.2/13.1	$1.35 \times 2.76 \times 0.14$ (VP-5/HP-4)	Dual	SIW/Dipole
[18]	2023	26	33	11.9/11.6*	$0.14^* \times 2.04 \times 0.5$ (4)	Dual	ME dipole/ ME dipole
[20]	2022	27	18.5	10.3/11.3	$0.41 \times 2.61 \times 0.2$ (4)	Dual	Cavity/Slot
[24]	2024	26.9	3.7	-	-	Single	-/DRA
[25]	2021	32.4	47.1	11.4/-	$0.55 \times 1.60 \times 0.21$ (4)	Single	DRA/-
[26]	2022	28	13.2	12.5	$0.50 \times 2.97 \times 0.23$ (6)	Single	DRA/-
This work	**-**	**28**	**13.3**	**10.0/10.1**	**$0.51 \times 1.99 \times 0.23$ (4)**	**Dual**	**DRA/DRA**

λ_0 is the wavelength in the vacuum at the center frequency. $*$: without feeding structure.

4.3. Discussion

Table 1 provides a comparison between the proposed antenna and other endfire antennas. The designs in [15–18, 20] can successfully achieve endfire dual-polarized radiation and beam scanning. However, the plane size in [15–17] is large while the profile in [18] is high. In [20], the radiation pattern is tilted. In [24–26], an endfire antenna with beam scanning function is realized by using a DRA, but only single-polarized (VP or HP) radiation can be achieved. In this design, an effective design method is presented for the dual-polarized endfire substrate integrated DRA, filling the gap that there is no DRA array to achieve endfire dual polarizations for millimeter wave.

5. CONCLUSION

In this work, a compact dual-polarized endfire DRA array has been proposed, fabricated, and experimentally validated. Each antenna element integrates a DRA with an open-ended cavity, and two sets of orthogonal DRA and cavity modes are employed to realize VP and HP polarizations. Building on the single-element design, a four-element linear array was implemented. Measurement results show good agreement with simulations, confirming that the array maintains stable performance for both polarizations. The proposed antenna demonstrates significant potential for millimeter-wave 5G terminal applications, offering compact size, dual-polarized operation, and beam-steering capability.

ACKNOWLEDGEMENT

This work was supported by the Talent Introduction Project of Nanjing University of Industry Technology under Grant YK23-03-05 and Nantong University under Grant 135424630060.

REFERENCES

[1] Chettri, L. and R. Bera, "A comprehensive survey on Internet of Things (IoT) toward 5G wireless systems," *IEEE Internet of Things Journal*, Vol. 7, No. 1, 16–32, 2020.

[2] Tahir, M., M. H. Habaebi, M. Dabbagh, A. Mughees, A. Ahad, and K. I. Ahmed, "A review on application of blockchain in 5G and beyond networks: Taxonomy, field-trials, challenges and opportunities," *IEEE Access*, Vol. 8, 115 876–115 904, 2020.

[3] Feng, B., L. Li, K. L. Chung, and Y. Li, "Wideband widebeam dual circularly polarized magnetoelectric dipole antenna/array with meta-columns loading for 5G and beyond," *IEEE Transactions on Antennas and Propagation*, Vol. 69, No. 1, 219–228, 2020.

[4] Ivashina, M., A. Vilenskiy, H.-T. Chou, J. Oberhammer, and M. N. M. Kehn, "Antenna technologies for beyond-5G wireless communication: Challenges and opportunities," in *2021 International Symposium on Antennas and Propagation (ISAP)*, 1–2, Taipei, Taiwan, 2021.

[5] Zhang, J., X. Ge, Q. Li, M. Guizani, and Y. Zhang, "5G millimeter-wave antenna array: Design and challenges," *IEEE Wireless Communications*, Vol. 24, No. 2, 106–112, 2016.

[6] Naqvi, A. H. and S. Lim, "Review of recent phased arrays for millimeter-wave wireless communication," *Sensors*, Vol. 18, No. 10, 3194, 2018.

[7] Sadhu, B., Y. Tousi, J. Hallin, S. Sahl, S. K. Reynolds, O. Renström, K. Sjögren, O. Haapalahti, N. Mazor, B. Bokinge, G. Weibull, H. Bengtsson, A. Carlinger, E. Westesson, J.-E. Thillberg, L. Rexberg, M. Yeck, X. Gu, M. Ferriss, D. Liu, D. Friedman, and A. Valdes-Garcia, "A 28-GHz 32-element TRX phased-array IC with concurrent dual-polarized operation and orthogonal phase and gain control for 5G communications," *IEEE Journal of Solid-state Circuits*, Vol. 52, No. 12, 3373–3391, 2017.

[8] Dunworth, J. D., A. Homayoun, B.-H. Ku, Y.-C. Ou, K. Chakraborty, G. Liu, T. Segoria, J. Lerdworatawee, J. W. Park, H.-C. Park, H. Hedayati, D. Lu, P. Monat, K. Douglas, and V. Aparin, "A 28 GHz bulk-CMOS dual-polarization phased-array transceiver with 24 channels for 5G user and basestation equipment," in *2018 IEEE International Solid-state Circuits Conference-(ISSCC)*, 70–72, Francisco, CA, USA, 2018.

[9] Moreno, R. M., J. Ala-Laurinaho, A. Khripkov, J. Ilvonen, and V. Viikari, "Dual-polarized mm-Wave endfire antenna for mobile devices," *IEEE Transactions on Antennas and Propagation*, Vol. 68, No. 8, 5924–5934, 2020.

[10] Moreno, R. M., J. Kurvinen, J. Ala-Laurinaho, A. Khripkov, J. Ilvonen, J. van Wonterghem, and V. Viikari, "Dual-polarized mm-Wave endfire chain-slot antenna for mobile devices," *IEEE Transactions on Antennas and Propagation*, Vol. 69, No. 1, 25–34, 2020.

[11] Hsu, Y.-W., T.-C. Huang, H.-S. Lin, and Y.-C. Lin, "Dual-polarized quasi Yagi-Uda antennas with endfire radiation for millimeter-wave mimo terminals," *IEEE Transactions on Antennas and Propagation*, Vol. 65, No. 12, 6282–6289, 2017.

[12] Lu, R., C. Yu, Y. Zhu, and W. Hong, "Compact millimeter-wave endfire dual-polarized antenna array for low-cost multibeam applications," *IEEE Antennas and Wireless Propagation Letters*, Vol. 19, No. 12, 2526–2530, 2020.

[13] Zhang, J., K. Zhao, L. Wang, S. Zhang, and G. F. Pedersen, "Dual-polarized phased array with end-fire radiation for 5G handset applications," *IEEE Transactions on Antennas and Propagation*, Vol. 68, No. 4, 3277–3282, 2019.

[14] Li, H., Y. Li, L. Chang, W. Sun, X. Qin, and H. Wang, "A wideband dual-polarized endfire antenna array with overlapped apertures and small clearance for 5G millimeter-wave applications," *IEEE Transactions on Antennas and Propagation*, Vol. 69, No. 2, 815–824, 2020.

[15] Li, Y., F. Wu, D. Xi, Z. Jiang, C. Yu, and W. Hong, "A compact dual-polarized endfire antenna array for 5G millimeter-wave terminal," *IEEE Antennas and Wireless Propagation Letters*, Vol. 22, No. 6, 1466–1470, 2023.

[16] Zhu, Y. and C. Deng, "Wideband dual-polarized endfire phased array antenna with small ground clearance for 5G mmWave mobile terminals," *IEEE Transactions on Antennas and Propagation*, Vol. 71, No. 6, 5469–5474, 2023.

[17] Zhu, Y., H. Xu, and C. Deng, "Single-layer dual-polarized endfire phased array antenna for 5G mm-Wave mobile terminals," *IEEE Antennas and Wireless Propagation Letters*, Vol. 23, No. 6, 1939–1943, 2024.

[18] Guo, Y., Y. Li, J. Wang, and L. Ge, "A compact substrate-integrated dual-polarized magneto-electric dipole antenna with endfire radiation for millimeter-wave applications," *IEEE Transactions on Antennas and Propagation*, Vol. 71, No. 10, 8332–8337, 2023.

[19] Sun, K., B. Wang, T. Yang, S. Liu, Y. Chen, Y. Zhao, and D. Yang, "Dual-polarized millimeter-wave endfire array based on substrate integrated mode-composite transmission line," *IEEE Transactions on Antennas and Propagation*, Vol. 70, No. 1, 341–352, 2021.

[20] Sun, L., Y. Li, and Z. Zhang, "Wideband dual-polarized endfire antenna based on compact open-ended cavity for 5G mm-Wave mobile phones," *IEEE Transactions on Antennas and Propagation*, Vol. 70, No. 3, 1632–1642, 2021.

[21] Zhao, C. X., Y. M. Pan, and G. D. Su, "Design of filtering dielectric resonator antenna arrays using simple feeding networks," *IEEE Transactions on Antennas and Propagation*, Vol. 70, No. 8, 7252–7257, 2022.

[22] Liu, Y.-T. and K. W. Leung, "28 GHz substrate-integrated filtering dielectric resonator antenna array," *IEEE Transactions on Antennas and Propagation*, Vol. 70, No. 10, 9900–9905, 2022.

[23] Yang, M.-D., Y.-M. Pan, Y.-X. Sun, and K.-W. Leung, "Wideband circularly polarized substrate-integrated embedded dielectric resonator antenna for millimeter-wave applications," *IEEE Transactions on Antennas and Propagation*, Vol. 68, No. 2, 1145–1150, 2019.

[24] Shi, J., Y. Guo, R. Zhao, B. Wu, Y. Chen, and W. Zhang, "Endfire substrate integrated dielectric resonator antenna with dual-beam radiation for millimeter-wave application," *IEEE Antennas and Wireless Propagation Letters*, Vol. 23, No. 5, 1523–1527, 2024.

[25] Omar, A. A., J. Park, W. Kwon, and W. Hong, "A compact wideband vertically polarized end-fire millimeter-wave antenna utilizing slot, dielectric, and cavity resonators," *IEEE Transactions on Antennas and Propagation*, Vol. 69, No. 9, 5234–5243, 2021.

[26] Yang, W.-W., X.-H. Ding, T.-W. Chen, L. Guo, W. Qin, and J.-X. Chen, "A shared-aperture antenna for (3.5, 28) GHz terminals with end-fire and broadside steerable beams in millimeter wave band," *IEEE Transactions on Antennas and Propagation*, Vol. 70, No. 10, 9101–9111, 2022.

[27] Cui, L.-X., X.-H. Ding, W.-W. Yang, L. Guo, L.-H. Zhou, and J.-X. Chen, "Communication compact dual-band hybrid dielectric resonator antenna for 5G millimeter-wave applications," *IEEE Transactions on Antennas and Propagation*, Vol. 71, No. 1, 1005–1010, 2023.